



## Article

# The Effects of Microalloying on the Precipitation Behavior and Strength Mechanisms of X80 High-Strength Pipeline Steel under Different Processes

Guoqiang Ma <sup>1,†</sup>, Yimian Chen <sup>1,†</sup>, Guilin Wu <sup>1,2,\*</sup> , Shuize Wang <sup>1,2,\*</sup>, Tianyi Li <sup>3,4</sup>, Wenye Liu <sup>3,4</sup>, Honghui Wu <sup>1,2</sup>, Junheng Gao <sup>1,2</sup>, Haitao Zhao <sup>1,2</sup>, Chaolei Zhang <sup>1,2</sup>  and Xinping Mao <sup>1,2</sup>

<sup>1</sup> Institute for Carbon Neutrality, University of Science and Technology Beijing, Beijing 100083, China

<sup>2</sup> Beijing Advanced Innovation Center for Materials Genome Engineering, University of Science and Technology Beijing, Beijing 100083, China

<sup>3</sup> State Key Laboratory of Metal Materials for Marine Equipment and Application, Anshan 114009, China

<sup>4</sup> Ansteel Beijing Research Institute Co., Ltd., Beijing 102200, China

\* Correspondence: guilinwu@ustb.edu.cn (G.W.); wangshuize@ustb.edu.cn (S.W.);  
Tel.: +86-191-1201-0604 (G.W.)

† These authors contributed equally to this work.

**Abstract:** Pipeline steel is a special type of steel used for transporting, for example, oil and natural gas. This study focuses on X80-grade pipeline steel modified with the addition of Nb and Nb-V at different cooling rates (air cooling or quenching) after hot rolling and subjecting it to quenching and tempering heat treatment. Based on multiscale characterization techniques, the effects of microalloying and the cooling rate after hot rolling on the microstructure, precipitation behavior, and strengthening mechanisms were studied. The results showed that the strengths of quenched steels were higher than those of air-cooled steels, and the increase in strength was more pronounced with the addition of Nb-V than with the addition of Nb alone in the steels. Under the same cooling condition, the strengths of Nb-V-added steels were larger than those of Nb-added steels. Additionally, the Nb-V addition promotes the formation of lath structures. The yield stress of the steels, calculated by using measured microstructural parameters following the linear addition of strengthening, is in good agreement with the measured values.

**Keywords:** pipeline steel; microalloying; quenching and tempering; precipitation strengthening; Hall–Petch relationship



**Citation:** Ma, G.; Chen, Y.; Wu, G.; Wang, S.; Li, T.; Liu, W.; Wu, H.; Gao, J.; Zhao, H.; Zhang, C.; et al. The Effects of Microalloying on the Precipitation Behavior and Strength Mechanisms of X80 High-Strength Pipeline Steel under Different Processes. *Crystals* **2023**, *13*, 714. <https://doi.org/10.3390/cryst13050714>

Academic Editor: Pavel Lukáč

Received: 3 April 2023

Revised: 17 April 2023

Accepted: 19 April 2023

Published: 23 April 2023



**Copyright:** © 2023 by the authors. Licensee MDPI, Basel, Switzerland. This article is an open access article distributed under the terms and conditions of the Creative Commons Attribution (CC BY) license (<https://creativecommons.org/licenses/by/4.0/>).

## 1. Introduction

Pipeline transportation, the most economical and efficient means of transportation, is increasingly used as the demand for oil and thermal energy grows [1–5]. According to the API 5L standard, the most common pipeline steel grades are X42, X52, X60, and X65 [6–8]. To improve the transportation efficiency, and to use pipelines under high pressure, high temperature, low temperature, and other extreme environments, pipeline engineering has shifted toward the direction of large diameter, high pressure development. The comprehensive properties of pipeline steel, such as strength, low temperature toughness, and weldability, need to be further improved. It is urgent to research and develop new high-strength pipeline steels [3,9–11].

The API 5L high grade of X80 pipeline steel is the most mature steel with the highest strength level in the practical application field of natural gas and oil transmission worldwide [12,13]. Microalloy additions are critical for obtaining optimum properties in pipeline steel. For X80 pipeline steel, microalloying elements such as Ti, Nb, and V are used to obtain excellent microstructures combined with thermal mechanical control processing (TMCP). The comprehensive mechanical properties, such as high strength and high toughness, are thus obtained at a lower carbon equivalent [14–16]. In the process of controlled rolling and

controlled cooling, a large number of fine carbon–nitride precipitation containing Ti, Nb, and V is precipitated and can improve the mechanical properties of steel by postponing the recrystallization and grain growth of austenite grains to refine the grain, as well as by increasing the precipitation strengthening. In addition to ferritic steels, the practice of microalloying is also adopted in the case of austenitic alloys to improve their creep life [17]. Therefore, the microstructure and properties of steel can be effectively improved by controlling the precipitation behavior of Ti, Nb, and V microalloying elements through optimized processing technology [16,18,19].

For example, Zhao et al. [20] showed that dendritic precipitates in the as-cast steel slabs precipitate mainly at grain boundaries, and these dendritic precipitates dissolved and re-precipitated into two kinds of carbonitrides: Ti and Nb-rich (Ti, Nb)(C, N) carbonitrides during reheating. Wu et al. [14] reported the influence of finish rolling temperatures and tempering temperatures on microstructure and mechanical properties, and found that there were more granular bainite and strain-induced TiC precipitates in the quenched microstructure. Meanwhile, smaller sized polygonal ferrite grains were obtained in tempered microstructure with decreasing finish rolling temperatures. Gomez et al. [21] studied the effect of rolling temperature and austenite strengthening obtained at the end of thermomechanical processing on final microstructure and precipitation state, and found that ferrite grains were finer and more equiaxed when the austenite was more severely deformed during finishing. Lu et al. [15] investigated the microstructure features of a series of microalloyed steels using multiscale characterization techniques and adopted a chemical dissolution technique to extract the precipitates in the steels to quantify the individual strengthening contributions from grain size effects, solid-solution strengthening, and precipitation strengthening to understand fully the strengthening mechanisms for these steels. Zhao et al. [16] obtained desirable microstructural constituents consisting of acicular ferrite (AF), bainitic ferrite (BF), and degenerate martensite/austenite (M/A) at the high coiling temperature of 500 °C, and a high content of nano-sized (Nb, Ti)C precipitates formed because of the higher coiling temperature and auto-tempering induced by the re-reddening effect.

Nb element is widely used in the microalloying of pipeline steel. However, Nb-microalloyed pipeline steel is generally rolled in the austenite non-recrystallization zone, where the rolling temperature is low and the rolling reduction is large, which has higher requirements of rolling mill equipment [22–24]. It was found that the V-microalloyed pipeline steel could be rolled in the austenite recrystallization temperature area. The repeated recrystallization of austenite at high temperatures can be used to obtain fully refined austenite grains through multiple passes rolling, and the carbon–nitride precipitation formed in austenite can be used to promote the ferritic nucleation in the grains. After the phase transformation, a similar grain refinement as in Nb-microalloyed pipeline steel can be obtained [14,25,26]. It was also found that the properties of V-microalloyed pipeline steel can be significantly improved under quenching and tempering processing. To further improve the mechanical properties, the compositely added Nb-V and TMCP-accompanied tempering processes were used to achieve the sufficient precipitation strengthening of Nb and V. This method can not only meet the requirements of strength, but can also improve the shape of steel plate. In addition, the optimum microalloying composition design and the suitable accelerated cooling after hot rolling will lead to a better toughness property of X80 pipeline steel [27]. However, there are no detailed studies on the effects of microalloying and cooling rates on the precipitation behavior and strengthening mechanism of X80 pipeline steel after quenching and tempering treatment.

In this paper, two microalloying compositions of pipeline steels were designed, namely, Nb- and Nb-V-microalloyed X80 pipeline steel. Two cooling conditions of air cooling or quenching followed by quenching and tempering treatments respectively were adopted to the steels after hot rolling. The microstructure, precipitation behavior, and strengthening mechanism of the steels microalloyed with Nb and Nb-V with different cooling conditions were studied.

## 2. Materials and Methods

The components of two X80 pipeline steels microalloyed with Nb and Nb-V used in this study are shown in Table 1: the Nb-microalloyed X80 pipeline steel, which contains 0.06 wt.% Nb element (hereinafter referred to as X6Nb), and the Nb-V microalloyed X80 pipeline steel, which is based on X6Nb chemical composition by adding 0.06 wt.% V element (hereinafter referred to as X6Nb6V).

**Table 1.** Chemical composition of two experimental steels (mass fraction, %).

Samples	C	Si	Mn	Ni	Cr	Cu	Ti	Nb	V	Mo	Al	Fe
X6Nb	0.07	0.25	1.75	0.2	0.2	0.15	0.03	0.06	0	0.2	0.03	Bal.
X6Nb6V	0.07	0.25	1.75	0.2	0.2	0.15	0.03	0.06	0.06	0.2	0.03	Bal.

The two experimental steels were rolled at 1100 °C. Two slabs were rolled with thickness reduction from 25 mm to 3 mm after 5 passes of rolling followed by air cooling or water quenching, respectively, and the final size of the rolled plates was 3 mm × 50 mm × 200 mm. Subsequently, samples were cut from the plates and were processed by quenching and tempering. The quenching and tempering processing was as follows: the samples were placed in a high-temperature box furnace, held at 950 °C for 8 min, then water quenched, placed in a tube furnace, and held at 600 °C for 15 min. The hot-working process of experimental steels is illustrated in Figure 1.

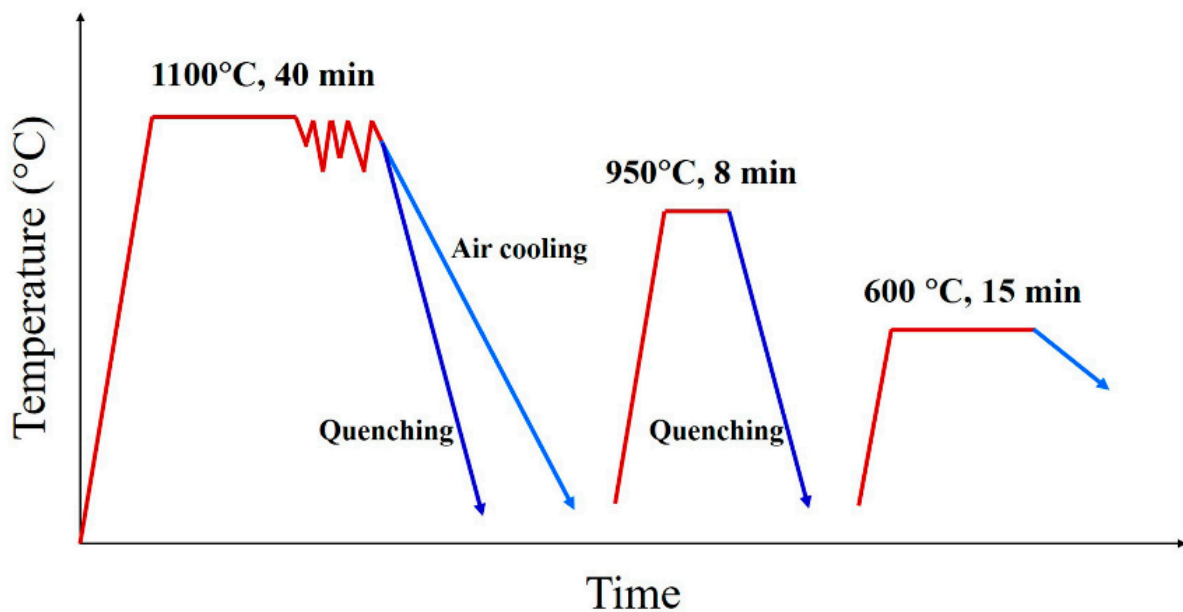


**Figure 1.** Schematic diagram of the hot-working process of experimental steels.

The quenched and tempered X80 pipeline steels were cut into tensile samples parallel to the rolling direction (gauge dimensions of 50 mm long, 12.5 mm wide and 1.8 mm thick). Tensile tests were carried out at a constant strain rate of  $1 \times 10^{-3} \text{ s}^{-1}$  on a Zwick Roell Z250 tensile tester. To prevent potential damage when the testing sample fractured, the mechanical extensometer was removed when the tensile strain reached 1.5%. The yield stress values ( $\sigma_y$ ) were calculated with the 0.2% offset method or measured at the lower yield point following the yield drop. The ultimate tensile stress ( $\sigma_{UTS}$ ) is the maximum stress during tensile.

The quenched and tempered samples were characterized by multiscale characterization techniques with scanning electron microscope (SEM), electron backscatter diffraction (EBSD), and transmission electron microscope (TEM). The compositions of  $\text{Fe}_3\text{C}$  and pre-

cipitates were analyzed and deduced by energy dispersive spectroscopy (EDS) equipped on the TEM. A D8-Advance X-ray diffraction (XRD) meter with Cu  $K_{\alpha}$  radiation operating at 40 kV and 150 mA was employed to measure the dislocation density. The glancing angles ranged from  $35^{\circ}$  to  $140^{\circ}$  with a  $0.02^{\circ}$  scanning step timing 1 s per step. SEM samples were ground from 320 to 2000 grit abrasive papers, then mechanically polished, and finally eroded for about 30 s in a solution of nitric acid and ethyl alcohol (4:96 by volume). EBSD samples were ground by 2000 grit abrasive papers, and then polished in a mixture of perchloric acid and ethyl alcohol (6:94 by volume) at room temperature. The polishing parameters were a voltage of 20 V and a polishing time of 30 s. TEM foils were prepared by a conventional twin-jet technique in the solutions consistent with EBSD preparing at 253 K. The foils were characterized in a JEOL-2100 TEM operating at 200 KV.

### 3. Results

Under air-cooling conditions, the microstructures in the X6Nb and X6Nb6V after quenching and tempering (hereinafter referred to as X6Nb-air-cooled and X6Nb6V-air-cooled samples) are shown in Figure 2. It can be found that the steels are tempered sorbite after quenching and high-temperature tempering. The microstructures of both steels are composed of polygonal ferrite (PF), residual laths, and dot-shaped carbides. There are more large-size carbides and residual laths in the X6Nb6V-air-cooled sample compared to the X6Nb-air-cooled sample.

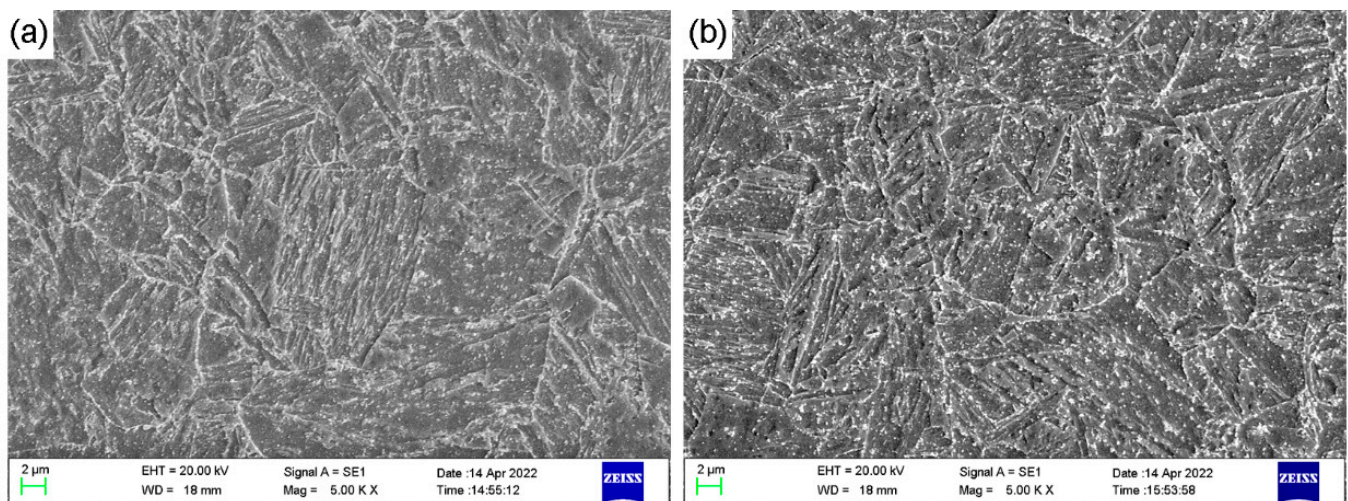


**Figure 2.** SEM observations showing the ferrites, precipitated  $Fe_3C$  and residual lath structures in the samples after quenching and tempering: (a) X6Nb-air-cooled sample, (b) X6Nb6V-air-cooled sample.

Under quenching conditions, the microstructures in the X6Nb and X6Nb6V after quenching and tempering (hereinafter referred to as X6Nb-quenched and X6Nb6V-quenched samples) are shown in Figure 3. The microstructures belong to tempered sorbite; however, the lath structures of the X6Nb-quenched sample and the X6Nb6V-quenched sample, in the microstructures, increase significantly compared to the samples under air-cooling conditions. The structure of polygonal ferrite is also significantly refined.

EBSD inverse pole figure (IPF) maps in the X6Nb-air-cooled sample and X6Nb6V-air-cooled sample after quenching and tempering are shown in Figure 4. The grains are of a typical polygonal shape. Under air-cooling conditions, the addition of V refines the grains slightly. The grain sizes were calculated by EBSD (determined from the EBSD data using a cut-off angle of  $15^{\circ}$ ) [28]. The grain size varies from submicron to dozens of microns and thus the standard deviations are large. The average grain sizes of the X6Nb-air-cooled sample and X6Nb6V-air-cooled sample are  $1.9 \pm 2.1 \mu m$  and  $1.8 \pm 2.0 \mu m$ , respectively.



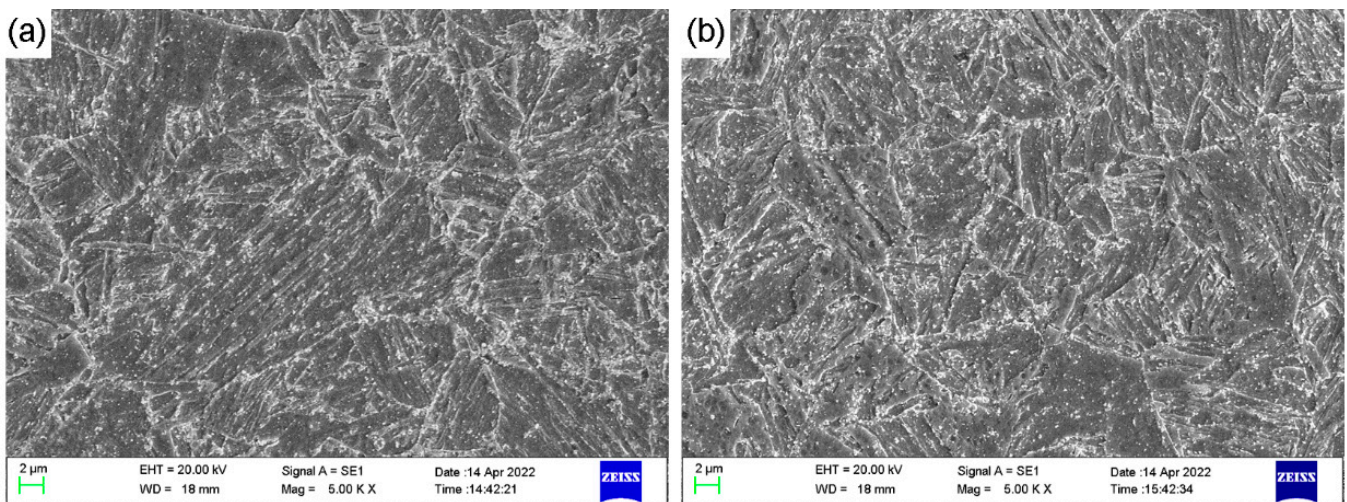


**Figure 3.** SEM observations showing the refined ferrites, precipitated  $\text{Fe}_3\text{C}$ , and more lath structures in the samples after quenching and tempering: (a) X6Nb-quenched sample, (b) X6Nb6V-quenched sample.

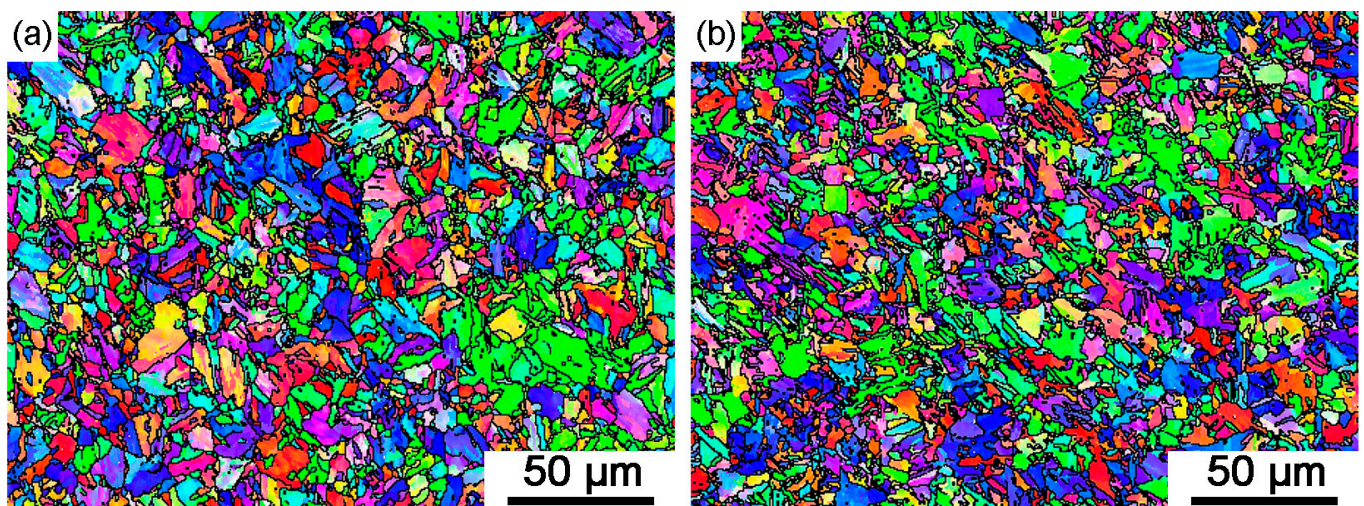


**Figure 4.** EBSD inverse pole figure (IPF) maps in the pipeline steels after quenching and tempering: (a) X6Nb-air-cooled sample, (b) X6Nb6V-air-cooled sample.

The IPF maps in the X6Nb-quenched sample and X6Nb6V-quenched sample after quenching and tempering are shown in Figure 5. Many grains were penetrated by the lath structure, and the grain morphologies are not typical of polygonal ferrite. Under air-cooling conditions, the addition of V still refines the grains slightly. The average grain sizes of the X6Nb-quenched sample and the X6Nb6V-quenched sample are  $1.5 \pm 1.8 \mu\text{m}$  and  $1.4 \pm 1.6 \mu\text{m}$ , respectively.

TEM foils of experimental steels were observed by high-resolution TEM. The observed microstructures in the X6Nb-air-cooled sample after quenching and tempering are shown in Figure 6. The microstructures are mainly lath structures, with high-density dislocations in the lath structures. Sub-micron  $\text{Fe}_3\text{C}$  exists in the microstructures, and the morphology of  $\text{Fe}_3\text{C}$  is a large block, which mostly exists at grain boundaries or the edge of laths. The nanoscale precipitates are evenly distributed and dispersed, and the size range of precipitates varies from a few nanometers to dozens of nanometers, and the precipitates' morphology is mainly spherical. It can be deduced from EDS measurements that the small precipitates consist mainly of (Nb, Ti)C.



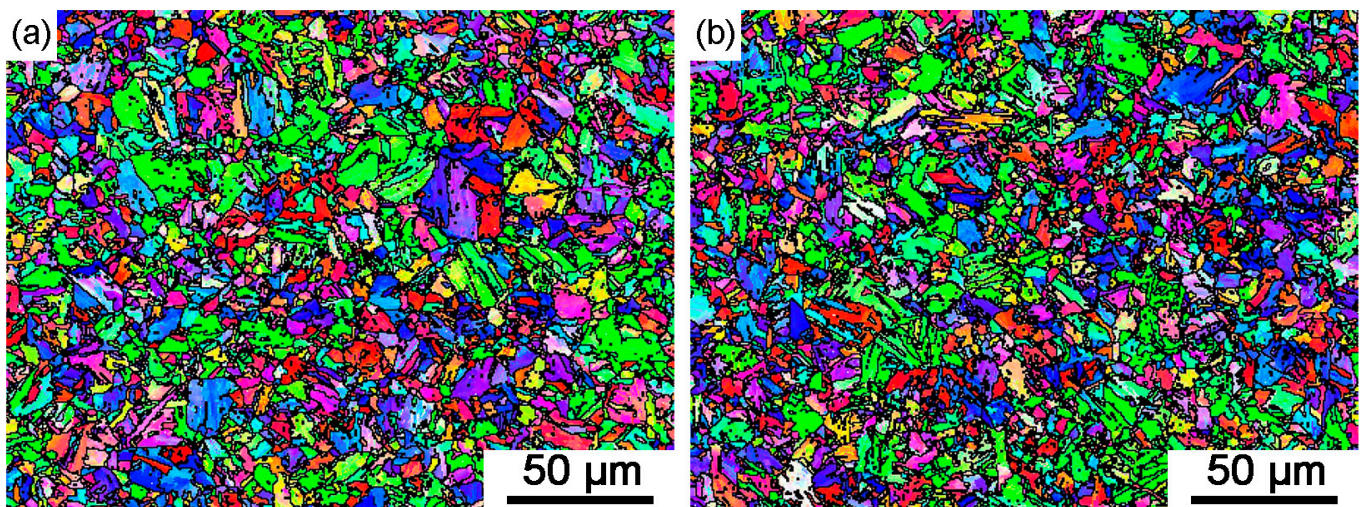


**Figure 5.** IPF maps in the pipeline steel after quenching and tempering: (a) X6Nb-quenched sample, (b) X6Nb6V-quenched sample.

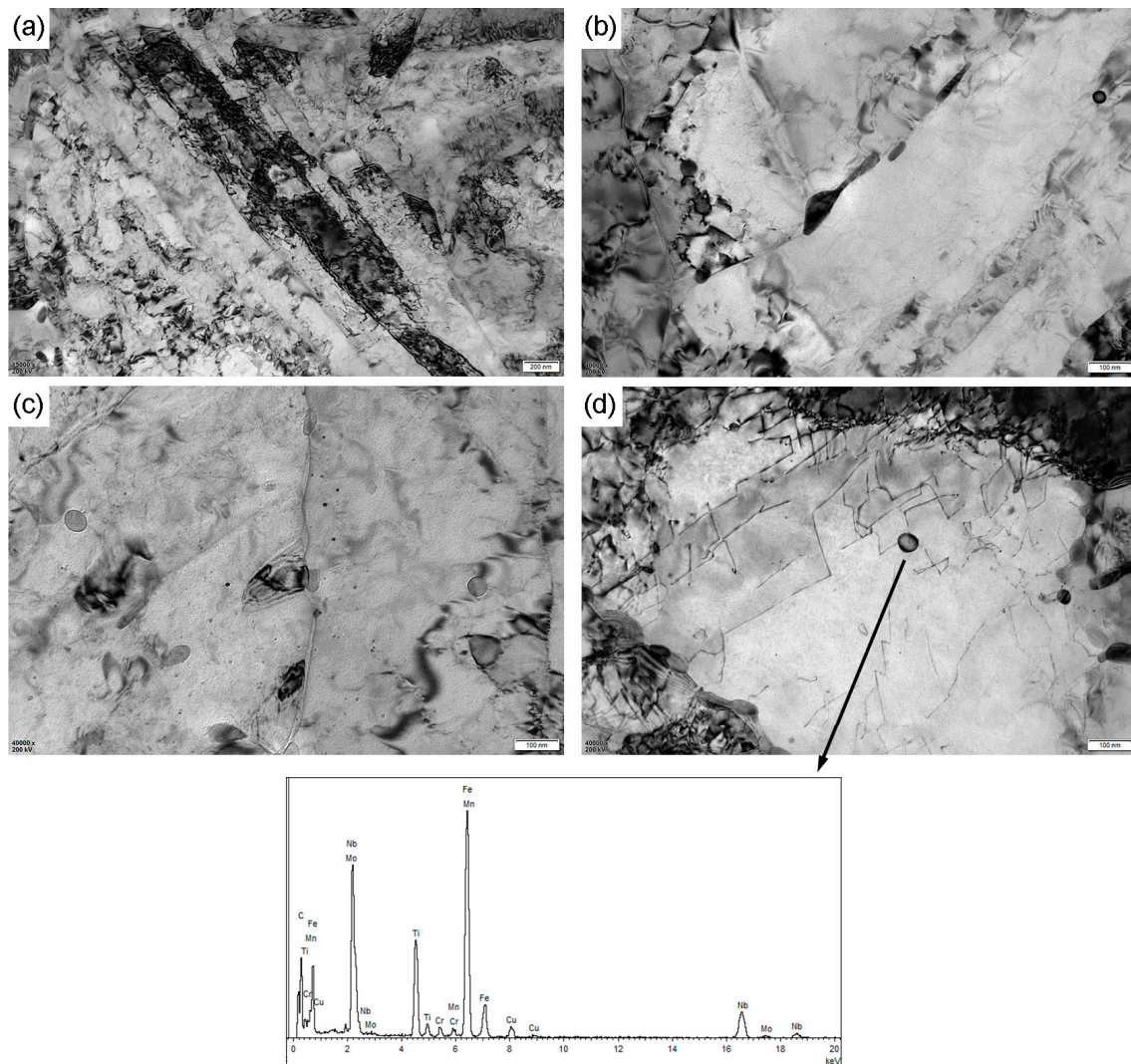


**Figure 6.** TEM-observed microstructures in the X6Nb-air-cooled sample after quenching and tempering: (a) high-density dislocations in lath structures, (b) sub-micron block  $\text{Fe}_3\text{C}$ , (c) nanoscale precipitates, and (d) composition of precipitates.



Microstructures in the X6Nb6V-air-cooled sample after quenching and tempering are shown in Figure 7. Lath structures with high-density dislocations, nanoscale precipitates, and sub-micron block  $\text{Fe}_3\text{C}$  are found in the microstructures. Compared with the X6Nb-air-cooled sample, the number of nanoscale precipitates has increased significantly, and the nanoscale precipitates are distributed more evenly in the X6Nb6V-air-cooled sample. The size variation range of precipitates is smaller, the precipitates' morphology is mainly spherical, and many precipitates can be observed precipitated along dislocations in the X6Nb6V-air-cooled sample. There is an obvious interaction with dislocation (Figure 7b). Such nanoscale precipitates can produce a pinning effect on dislocation, and effectively hinder dislocation slip and thus improve the mechanical properties of the structure. The small precipitates are mainly (Nb, Ti)C and VC deduced from EDS measurements.

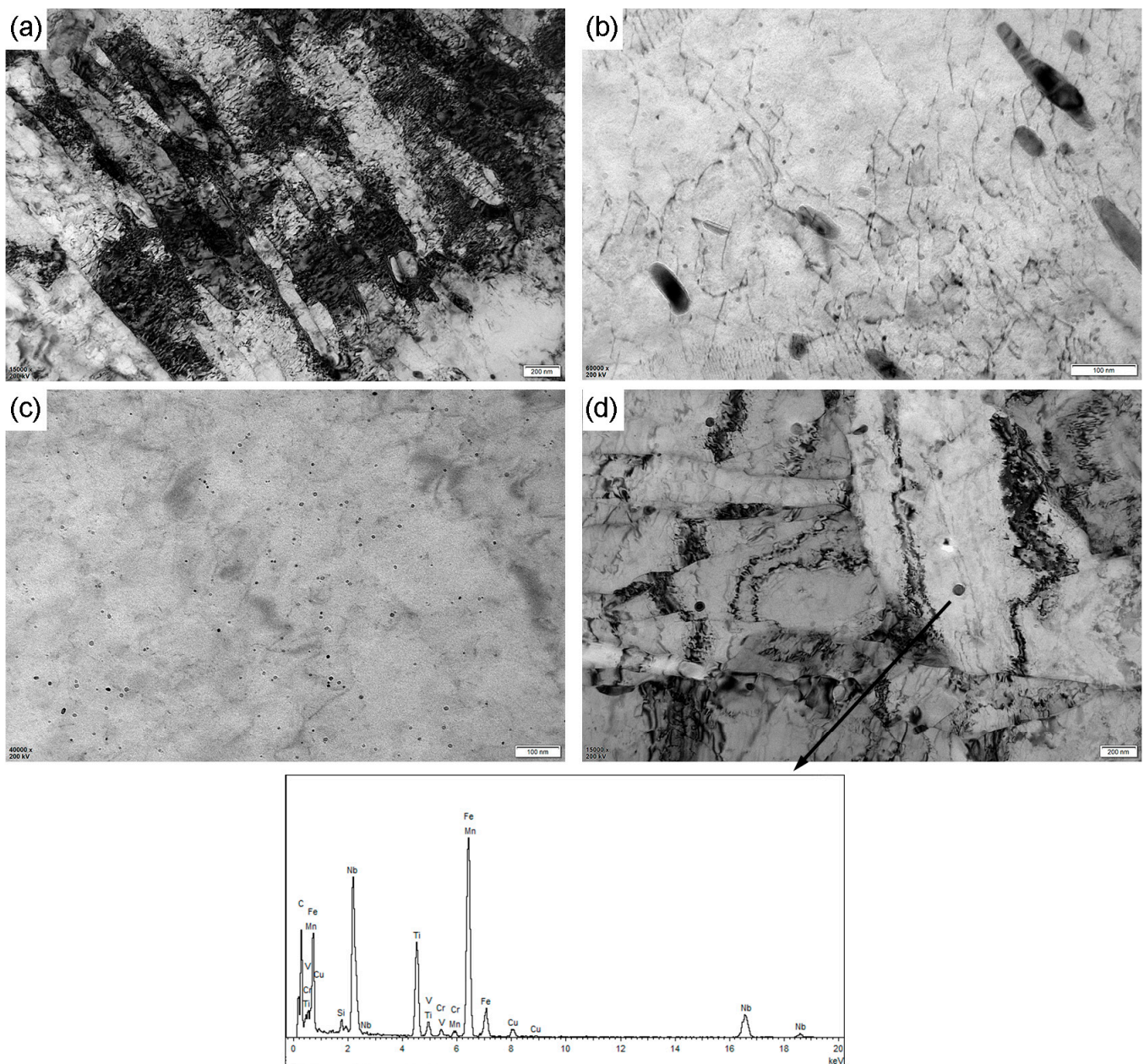


**Figure 7.** TEM-observed microstructures in the X6Nb6V-air-cooled sample after quenching and tempering: (a) high-density dislocations in lath structures, (b) sub-micron block  $\text{Fe}_3\text{C}$ , (c) more nanoscale precipitates, and (d) composition of precipitates.

The observed microstructures in the X6Nb-quenched sample after quenching and tempering are shown in Figure 8. Lath structures are the main features in the microstructures. The size range of precipitates varies from a few nanometers to dozens of nanometers, and the morphology of precipitates is mainly spherical, as seen in Figure 6. The small precipitates are mainly (Nb, Ti)C deduced from EDS measurements.

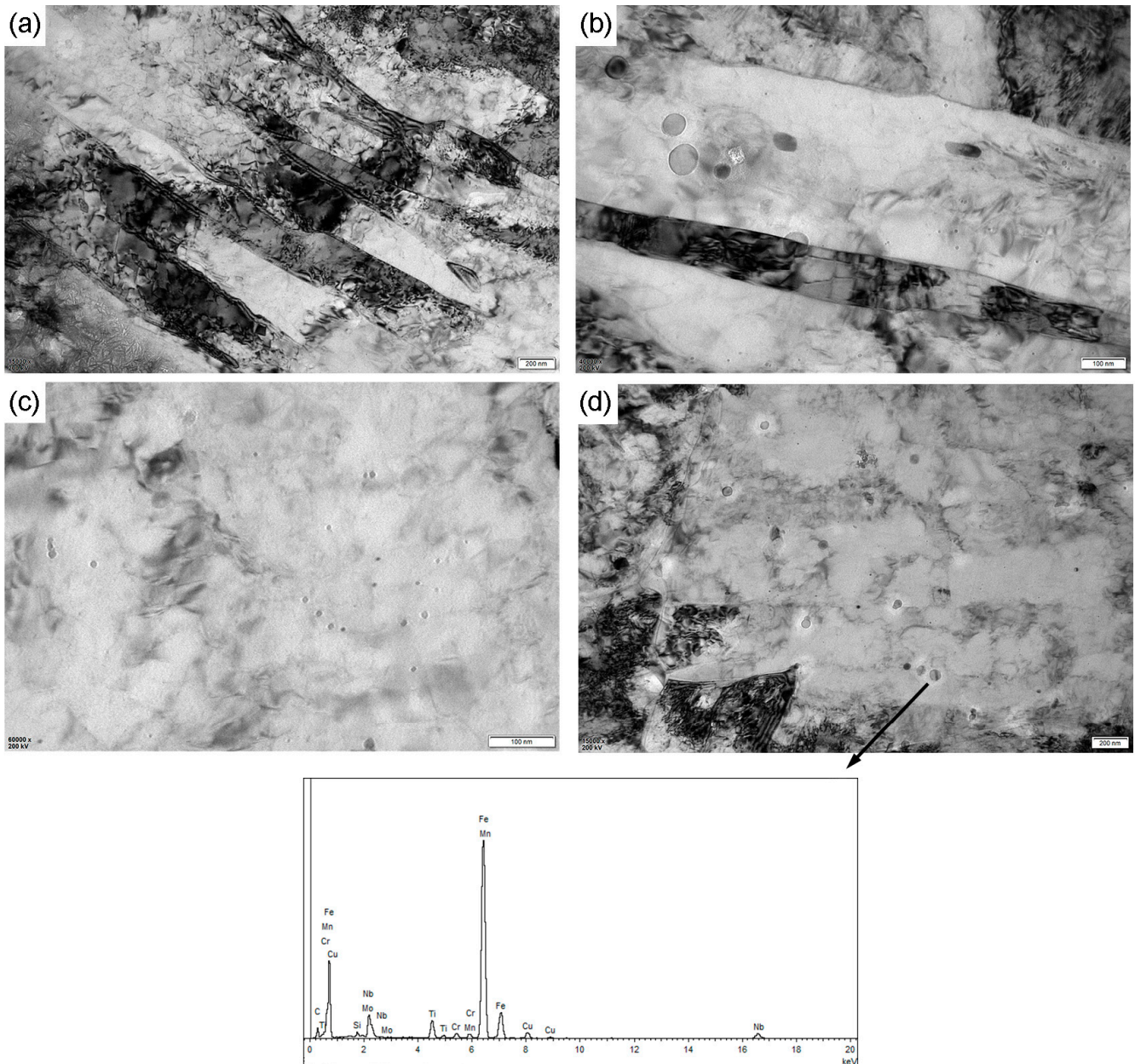


**Figure 8.** TEM-observed microstructures in the X6Nb-quenched sample after quenching and tempering: (a) high-density dislocations in lath structures, (b) sub-micron block Fe<sub>3</sub>C, (c) nanoscale precipitates, and (d) composition of precipitates.

Lath structures are still the main feature in the X6Nb6V-quenched sample after quenching and tempering, as shown in Figure 9. The Fe<sub>3</sub>C, precipitates, and composition of precipitates were deduced and analyzed.



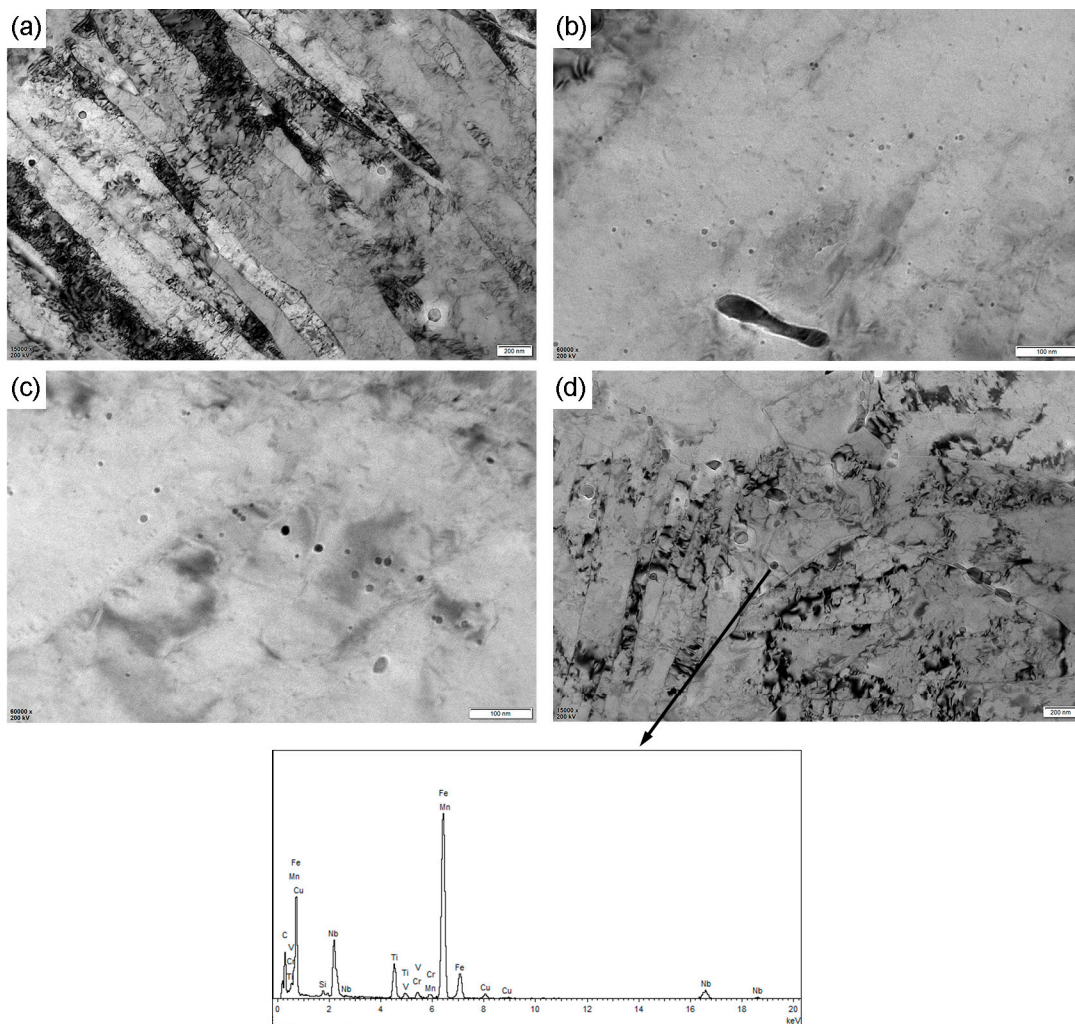


**Figure 9.** TEM-observed microstructures in the X6Nb6V-quenched sample after quenching and tempering: (a) high-density dislocations in lath structures, (b) sub-micron block Fe<sub>3</sub>C, (c) nanoscale precipitates, and (d) composition of precipitates.

#### 4. Discussion

The morphology and size distribution of precipitates in the steels after quenching and tempering were analyzed statistically by randomly selecting 20 fields of view at the same multiple. The size distributions of nanoscale precipitates are shown in Figure 10 and the average precipitate sizes are given in Table 2. According to statistics, it was found that the number of precipitates increases obviously in the microstructure whether under the conditions of air cooling or quenching when Nb-V is compositely added. The volume fraction ( $f$ ) of precipitates can be calculated according to the McCall–Boyd method [29,30]:

$$f = \left( \frac{1.4\pi}{6} \right) \times \left( \frac{Nd^2}{A} \right) \quad (1)$$

where the  $N$  is the amount of precipitates on the statistical fields of view,  $d$  is the average diameter of precipitates, and  $A$  is the size of the statistical fields of view. The volume fraction ( $f$ ) is also tabulated in Table 2. Under the air-cooling condition, the addition of Nb-V leads to a decrease in the average diameter of precipitates, but the volume fraction increases significantly, from 0.077% of the X6Nb-air-cooled sample to 0.2154% of the X6Nb6V-air-cooled sample in the microstructure. This finding is the same under the quenching condition, i.e., the addition of Nb-V decreases the average diameter of precipitates and increases the volume fraction. When V element is added to steel, the tempering process will cause V

atoms to participate during the diffusion and nucleate vanadium carbide at the matrix and/or boundaries in the microstructure. In general, precipitates smaller than 20 nm are generally vanadium carbide, and the vanadium carbide precipitates are usually spherical or nearly spherical. In addition, for the same microalloying in experimental steels, the volume fraction of precipitates is higher and the precipitates' size is smaller under quenching conditions.

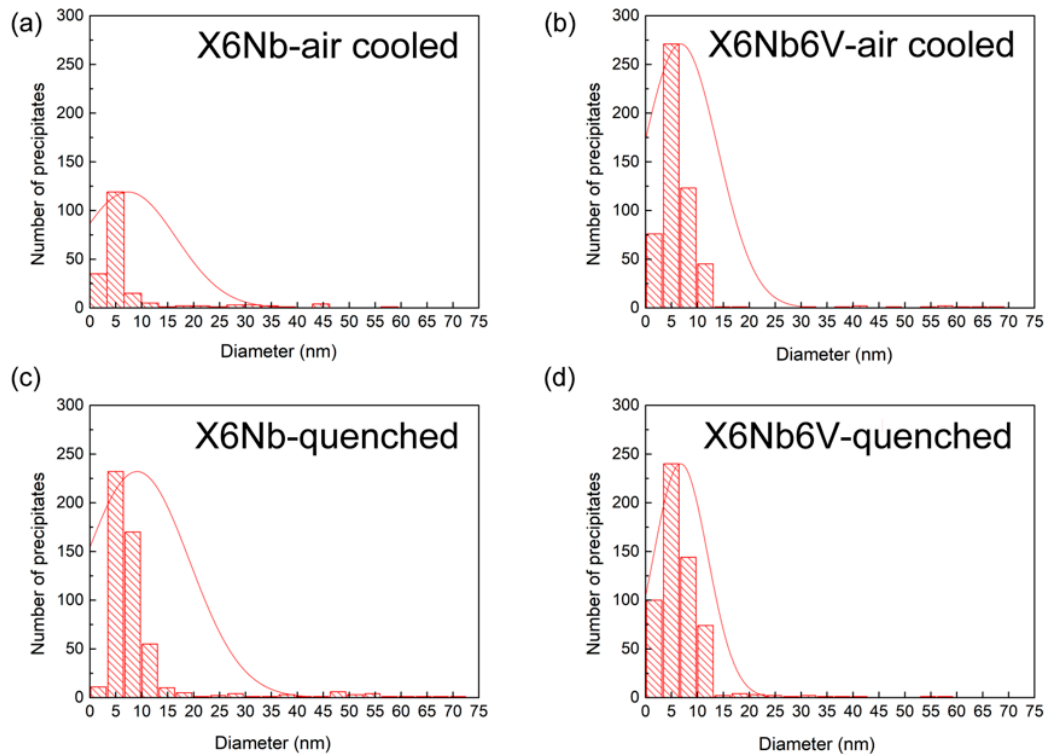


**Figure 10.** Size distributions of nanoscale precipitates in the samples after quenching and tempering: (a) X6Nb-air-cooled sample, (b) X6Nb6V-air-cooled sample, (c) X6Nb-quenched sample, (d) X6Nb6V-quenched sample.

**Table 2.** Statistical results of precipitates of experimental steels after quenching and tempering.

Conditions	Volume Fraction (f), %	Average Size (d), nm
X6Nb-air-cooled	0.0770	12.244
X6Nb6V-air-cooled	0.2154	9.895
X6Nb-quenched	0.1510	8.127
X6Nb6V-quenched	0.2230	6.936

The mechanical properties of the two experimental steels are shown in Table 3. It can be seen that the mechanical properties of both X6Nb and X6Nb6V meet the mechanical properties requirements of X80 pipeline steel specified in the API 5L standard. Whether under air cooling or quenching after hot rolling, it is obvious that the addition of Nb-V increases the yield strength and tensile strength of the experimental steels after quenching and tempering. For the same microalloying in the experimental steels, the tensile strength and yield strength of quenched and tempered steel under quenching conditions are both higher than those under air-cooling conditions. The strength of X6Nb6V increases more significantly.

**Table 3.** Mechanical properties of X80 pipeline steels after quenching and tempering.

Conditions	$\sigma_{UTS}$ (MPa)	$\sigma_y$ (MPa)
X6Nb-air-cooled	724	658
X6Nb6V-air-cooled	801	740
X6Nb-quenched	737	688
X6Nb6V-quenched	880	850

The strengthening mechanisms of present steels include precipitation strengthening, grain boundary strengthening, solid solution strengthening, and dislocation strengthening. Precipitation strengthening ( $\sigma_p$ ) can be derived based on the Ashby–Orowan model [31]:

$$\sigma_p = \left(0.538Gb f^{1/2}/d\right) \ln\left(\frac{d}{2b}\right) \quad (2)$$

where  $f$  is the volume fraction of particles,  $d$  is the diameter of particles,  $G$  is the shear modulus (78 GPa), and  $b$  is the Burgers vector magnitude (0.248 nm). When a slip dislocation is bypassing a non-deformable particle using the Orowan mechanism, the bending of the dislocation will increase the linear tension of the dislocation. Therefore, more applied stress is required to push the dislocation past the particle and continue to slip, resulting in the strengthening of the material. According to Equation (2), the strengthening effect of the particle is proportional to  $f^{1/2}$  and decreases with the increase in the particle's diameter ( $d$ ). Therefore, refining the size of the particles can significantly improve the precipitation strengthening effect when the particles have the same volume fraction ( $f$ ).

Grain boundary strengthening is based on boundaries, as dislocation glide barriers with a strength were found to be inversely proportional to the square root of the grain size, as can be described by the classical Hall–Petch relationship [32,33]:

$$\sigma_{GB} = K_{HP} D_{av}^{-1/2} \quad (3)$$

where  $K_{HP}$  is the slope of the straight line relating to the flow stress of a polycrystalline metal to the inverse square root of grain size, and  $D_{av}$  is the average grain size. For microalloy steel and plain carbon steel, many studies have reported  $K_{HP}$  values varying in a very broad range: from 120 MPa· $\mu\text{m}^{1/2}$  in interstitial free steel to 700 MPa· $\mu\text{m}^{1/2}$  in tempered steel [34–40]. These values are influenced by the content of alloying elements, the dislocation density, and other parameters. However, the value of  $K_{HP}$  as an indicator with boundaries as dislocation glide barriers cannot depend on the intragranular structural state. Therefore, it is necessary to accept the value typical for unalloyed and undeformed ferrite. In this work, the value of 400 MPa· $\mu\text{m}^{1/2}$  is adopted [37,38]. Note that this  $K_{HP}$  does not include the role of dislocation strengthening and other factors in grains.

The solid solution contents of Ti, Nb, and V in X80 pipeline steel after quenching and tempering were calculated according to the solubility product combined with the optimum chemical ratio. The results show that Ti, Nb, and V exist almost in the form of precipitates, and their solid solution content can be ignored. In addition to TiC, NbC, and VC, the C element in steel almost exists in the form of Fe<sub>3</sub>C particles during the 600 °C tempering process; the strengthening contribution of Fe<sub>3</sub>C is mainly precipitation strengthening, which is less than 20 MPa. The strengthening contribution of other elements in steel is assumed to be solid solution strengthening, and the calculation is consistent with the chemical composition in Table 1. Solid solution strengthening is normally expressed by the relationship:

$$\sigma_{ss} = \sum_{i=1}^n K_i C_i \quad (4)$$

where  $K_i$  is the intensity influencing factor of each individual element, and  $C_i$  represents the concentration of the elements [41].

As mentioned above, for the incomplete recrystallization structure, the strengthening contribution of dislocation density within the grain cannot be ignored [42,43]. The sample dislocation density was measured by XRD (Figure 11).

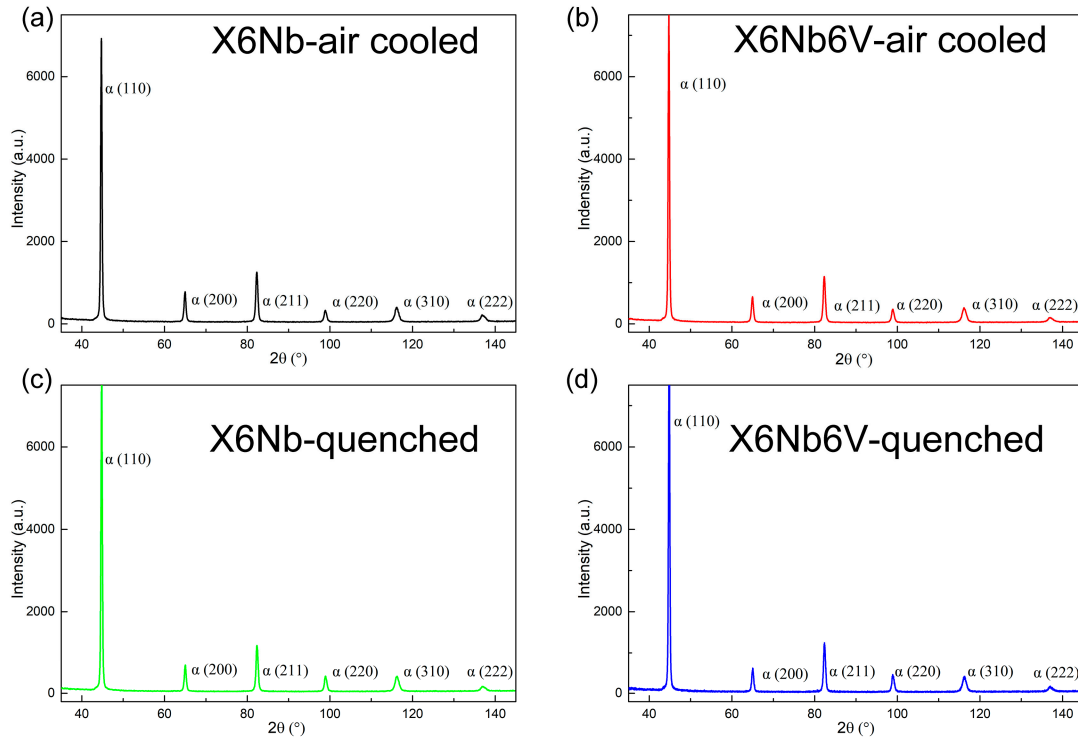


**Figure 11.** XRD results for dislocation density measurements in test steels after quenching and tempering: (a) X6Nb-air-cooled sample, (b) X6Nb6V-air-cooled sample, (c) X6Nb-quenched sample, (d) X6Nb6V-quenched sample.

The modified Williamson–Hall method was used to process the XRD results to obtain the dislocation density:

$$\Delta K_{tot} = \frac{0.9}{D_{av}} + \left( \frac{\pi E^2 b^2}{2} \right)^{\frac{1}{2}} \rho^{\frac{1}{2}} (KC^{1/2}) \quad (5)$$

where  $\Delta K_{tot}$  is the width of the XRD diffraction peak,  $E$  is a dimensionless constant,  $K$  is a constant taken equal to 0.9, and  $C$  is the average contrast factor of dislocation on the given crystallographic plane. The following Taylor formula was used to calculate the dislocation strengthening [41,44]:

$$\sigma_{dis} = M\alpha Gb\sqrt{\rho} \quad (6)$$

where  $M$  is the Taylor factor ( $M = 2.9$  for the random texture in bcc),  $\alpha$  is a constant taken to be 0.166,  $b$  is the Burgers vector magnitude, and  $G$  is the shear modulus. The calculated results show that the dislocation density increases with the addition of Nb-V compared to X6Nb. Under air-cooling conditions, the strengthening of the dislocation was 121 MPa and 132 MPa for X6Nb and X6Nb6V, respectively. Under quenching conditions, the strengthening of the dislocation was 138 MPa and 198 MPa for X6Nb and X6Nb6V, respectively. Based on additive law, where the total flow stress is calculated based on the measured microstructural parameters utilizing linearly addition, as shown in [39,42,44],

$$\sigma = \sigma_0 + \sigma_{ss} + \sigma_{dis} + \sigma_{GB} + \sigma_P + \sigma_{Fe3C} \quad (7)$$

where  $\sigma_0$  is the friction stress, taken to be 50 MPa for bcc Fe [36]. The dislocation density and calculated flow stress are shown in Table 4. The calculated results were in good agreement



with the measured values, showing an excellent match within <10%. The stress calculation method in this paper matches the tensile tests. The results in Table 4 for X80 pipeline steels make clear the robustness of the use of the measured microstructural parameters to predict flow stress. However, the calculation method can only predict the yield stress and does not predict the ultimate tensile stress. It is worth noting that the choice of  $K_{HP}$  is important since it can vary in a very broad range. The  $K_{HP}$  values are influenced by the content of alloying elements, the dislocation density, and other parameters. Therefore, it must be clarified what the  $K_{HP}$  refers to, and the typical value of the unalloyed and undeformed ferrite must be adopted. Based on this, the stress calculation can be more accurate.

**Table 4.** Calculated flow stresses utilizing the microstructure parameters and experimentally measured values from tensile tests.

Conditions	$\sigma_0$ (MPa)	$\sigma_{ss}$ (MPa)	$\sigma_p$ (MPa)	$\sigma_{Fe3C}$ (MPa)	$\sigma_{GB}$ (MPa)	$\sigma_{dis}$ (MPa)	$\rho$ (m <sup>-2</sup> )	$\sigma_{calculated}$ (MPa)	$\sigma_y$ (MPa)
X6Nb-air-cooled	50	82	76	16	290	121	$1.9 \times 10^{14}$	635	658
X6Nb6V-air-cooled	50	82	146	13	298	132	$2.3 \times 10^{14}$	721	740
X6Nb-quenched	50	82	139	17	327	138	$2.4 \times 10^{14}$	753	688
X6Nb6V-quenched	50	82	187	14	338	198	$5.0 \times 10^{14}$	869	850

Under the air-cooling condition, the addition of Nb-V leads to the decrease in the average diameter of precipitates, but the volume fraction increases significantly, from 0.077% of the X6Nb-air-cooled sample to 0.2154% of the X6Nb6V-air-cooled sample in the quenched and tempered microstructures. Under the air-cooling condition, the addition of Nb-V leads to precipitations providing an additional 70 MPa strengthening compared to X6Nb after quenching and tempering, while the additional precipitation strengthening is 48 MPa under the quenching condition. Under the same cooling condition, the increase in mechanical properties with the addition of Nb-V compared to the addition of Nb alone in pipeline steel was mainly attributed to the increase in precipitation strengthening after quenching and tempering. The precipitation and matrix microstructure jointly affected the mechanical properties of the quenched and tempered steel with the same microalloying under different cooling conditions.

## 5. Conclusions

Present X80 pipeline steels were modified with added Nb and Nb-V at different cooling rates after hot rolling and subjected to quenching and tempering treatments. The effects of microalloying and the cooling rate after hot rolling on the microstructure, precipitation behavior, and strengthening mechanism were investigated. The following conclusions were drawn:

- (1) The ultimate tensile stress and yield stress of the quenching condition steels are both higher than those of the air-cooling condition steels, and the increase in strength is more pronounced with the addition of Nb-V than with the addition of Nb alone in X80 pipeline steel.
- (2) Under the same cooling condition, the mechanical properties of Nb-V-added steel are better than those of Nb-added steel. Additionally, Nb-V-added steel has larger proportion of lath structure in the microstructure.
- (3) Based on measured microstructural parameters, the flow stress is rationalized utilizing linearly addition of the strengthening by solutes, precipitation, dislocation, and boundaries. The calculated results are in good agreement with the measured values.

**Author Contributions:** Data curation, G.M. and Y.C.; formal analysis, G.M., Y.C., H.W., J.G. and S.W.; investigation, G.M. and Y.C.; resources, H.Z., C.Z., T.L. and W.L.; supervision, G.W. and X.M.; writing—original draft, G.M., Y.C. and G.W.; writing—review and editing, G.M., S.W., X.M. and G.W. All authors have read and agreed to the published version of the manuscript.

**Funding:** This work was financially supported by the National Natural Science Foundation of China (NSFC, Nos. 52071038, 52122408, 52104369 and 52071023), the National State Key Research and Development Program (No. 2021YFB3702403).

**Institutional Review Board Statement:** Not applicable.

**Informed Consent Statement:** Not applicable.

**Data Availability Statement:** Not applicable.

**Conflicts of Interest:** The authors declare no conflict of interest.

## References

1. Hardie, D.; Charles, E.A.; Lopez, A.H. Hydrogen embrittlement of high strength pipeline steels. *Corros. Sci.* **2006**, *48*, 4378–4385. [[CrossRef](#)]
2. Zhang, G.A.; Cheng, Y.F. On the fundamentals of electrochemical corrosion of X65 steel in CO<sub>2</sub>-containing formation water in the presence of acetic acid in petroleum production. *Corros. Sci.* **2009**, *51*, 87–94. [[CrossRef](#)]
3. Dong, C.F.; Liu, Z.Y.; Li, X.G.; Cheng, Y.F. Effects of hydrogen-charging on the susceptibility of X100 pipeline steel to hydrogen-induced cracking. *Int. J. Hydrogen Energy* **2009**, *34*, 9879–9884. [[CrossRef](#)]
4. Arafin, M.A.; Szpunar, J.A. A new understanding of intergranular stress corrosion cracking resistance of pipeline steel through grain boundary character and crystallographic texture studies. *Corros. Sci.* **2009**, *51*, 119–128. [[CrossRef](#)]
5. Chen, Y.M.; Wang, S.Z.; Xiong, J.; Wu, G.L.; Gao, J.H.; Wu, Y.; Ma, G.Q.; Wu, H.H.; Mao, X.P. Identifying facile material descriptors for Charpy impact toughness in low-alloy steel via machine learning. *J. Mater. Sci. Technol.* **2023**, *132*, 213–222. [[CrossRef](#)]
6. Zhang, X.F.; Lin, M.; Okodi, A.; Tan, L.C.; Leung, J.Y.; Adeeb, S. Numerical Analysis of API 5 L X42 and X52 Vintage Pipes With Cracks in Corrosion Defects Using Extended Finite Element Method. *J. Press. Vess-T* **2021**, *143*, 143. [[CrossRef](#)]
7. Roccisano, A.; Nafisi, S.; Ghomashchi, R. Stress Corrosion Cracking Observed in Ex-service Gas Pipelines: A Comprehensive Study. *Metall. Mater. Trans. A* **2020**, *51*, 167–188. [[CrossRef](#)]
8. Zhao, Y.; Song, M. Failure Analysis of a Natural Gas Pipeline. *Eng. Fail. Anal.* **2016**, *63*, 61–71. [[CrossRef](#)]
9. Wang, L.; Zhou, P.S.; Hu, Y.W.; Wang, B. Microstructure and Impact Toughness Property of API X90 Heat-Affected Zones at Different Peak Temperatures. *J. Mater. Eng. Perform.* **2021**, *30*, 5787–5798. [[CrossRef](#)]
10. Yoo, J.-Y.; Ahn, S.S.; Seo, D.-H.; Song, W.-H.; Kang, K.-B. New Development of High Grade X80 to X120 Pipeline Steels. *Mater. Manuf. Process.* **2011**, *26*, 154–160. [[CrossRef](#)]
11. Wang, S.W.; Wang, S.Z.; Wu, H.H.; Wu, Y.; Mi, Z.L.; Mao, X.P. Towards enhanced strength-ductility synergy via hierarchical design in steels: From the material genome perspective. *Sci. Bull.* **2021**, *66*, 958–961. [[CrossRef](#)] [[PubMed](#)]
12. Wang, M.; Tan, M.Y.; Zhu, Y.; Huang, Y.; Xu, Y. Probing top-of-the-line corrosion using coupled multi-electrode array in conjunction with local electrochemical measurement. *Njp Mater. Degrad.* **2023**, *7*, 16. [[CrossRef](#)]
13. Gou, J.; Nie, R.; Xing, X.; Li, Z.; Cui, G.; Liu, J.; Deng, X.; Cheng, Y.F. Hydrogen-induced cracking of welded X80 steel studies by experimental testing and molecular dynamics modeling. *Corros. Sci.* **2023**, *214*, 111027. [[CrossRef](#)]
14. Wu, Q.; He, S.; Hu, P.; Liu, Y.; Zhang, Z.; Fan, C.; Fan, R.; Zhong, N. Effect of finish rolling temperature on microstructure and mechanical properties of X80 pipeline steel by on-line quenching. *Mater. Sci. Eng. A* **2023**, *862*, 144496. [[CrossRef](#)]
15. Lu, J.; Omotoso, O.; Wiskel, J.B.; Ivey, D.G.; Henein, H. Strengthening Mechanisms and Their Relative Contributions to the Yield Strength of Microalloyed Steels. *Metall. Mater. Trans. A* **2012**, *43*, 3043–3061. [[CrossRef](#)]
16. Zhao, J.; Hu, W.; Wang, X.; Kang, J.; Cao, Y.; Yuan, G.; Di, H.; Misra, R.D.K. A Novel thermo-mechanical controlled processing for large-thickness microalloyed 560MPa (X80) pipeline strip under ultra-fast cooling. *Mater. Sci. Eng. A* **2016**, *673*, 373–377. [[CrossRef](#)]
17. Guglielmino, E.; Pino, R.; Servetto, C.; Sili, A. Chapter 4—Creep damage of high alloyed reformer tubes. In *Handbook of Materials Failure Analysis with Case Studies from the Chemicals, Concrete and Power Industries*; Makhlof, A.S.H., Aliofkhaezraei, M., Eds.; Butterworth-Heinemann: Oxford, UK, 2016; pp. 69–91.
18. Zhao, M.-C.; Yang, K.; Shan, Y. The effects of thermo-mechanical control process on microstructures and mechanical properties of a commercial pipeline steel. *Mater. Sci. Eng. A* **2002**, *335*, 14–20. [[CrossRef](#)]
19. Zhao, M.-C.; Yang, K.; Xiao, F.-R.; Shan, Y.-Y. Continuous cooling transformation of undeformed and deformed low carbon pipeline steels. *Mater. Sci. Eng. A* **2003**, *355*, 126–136. [[CrossRef](#)]
20. Zhao, A.-M.; Wang, Y.; Chen, Y.-L.; Tang, D.; Gao, X.-T.; Zuo, B.-Q. Precipitation behaviors of X80 acicular ferrite pipeline steel. *Int. J. Min. Met. Mater.* **2011**, *18*, 309–313. [[CrossRef](#)]
21. Gomez, M.; Valles, P.; Medina, S.F. Evolution of microstructure and precipitation state during thermomechanical processing of a X80 microalloyed steel. *Mater. Sci. Eng. A* **2011**, *528*, 4761–4773. [[CrossRef](#)]
22. Li, H.; Liang, J.-L.; Feng, Y.-L.; Huo, D.-X. Microstructure transformation of X70 pipeline steel welding heat-affected zone. *Rare Met.* **2014**, *33*, 493–498. [[CrossRef](#)]
23. Patterson, T.; Lippold, J.C. Effect of niobium on the microstructure and properties of submerged arc welds in HSLA steel. *Weld. World* **2020**, *64*, 1089–1105. [[CrossRef](#)]

24. Sabokrouh, M.; Hashemi, S.H.; Farahani, M. Experimental study of the weld microstructure properties in assembling of natural gas transmission pipelines. *Proc. Inst. Mech. Eng. Part B J. Eng. Manuf.* **2015**, *231*, 1039–1047. [[CrossRef](#)]
25. Venkatsurya, P.K.C.; Jia, Z.; Misra, R.D.K.; Mulholland, M.D.; Manohar, M.; Hartmann, J.E. Understanding mechanical property anisotropy in high strength niobium-microalloyed linepipe steels. *Mater. Sci. Eng. A* **2012**, *556*, 194–210. [[CrossRef](#)]
26. Yang, C. *Principle and Application of Vanadium Steel Metallurgy*; Metallurgical Industry Press: Beijing, China, 2012.
27. Li, Z.; Liu, D.; Zhang, J.; Tian, W. Precipitates in Nb and Nb–V Microalloyed X80 Pipeline Steel. *Microsc. Microanal.* **2013**, *19*, 62–65. [[CrossRef](#)] [[PubMed](#)]
28. Chen, S.; Ma, G.; Wu, G.; Godfrey, A.; Huang, T.; Huang, X. Strengthening mechanisms in selective laser melted 316L stainless steel. *Mater. Sci. Eng. A* **2022**, *832*, 142434. [[CrossRef](#)]
29. Seher, R.J.; James, H.M.; Maniar, G.N. *Stereology and Quantitative Metallography*; ASTM International: West Conshohocken, PA, USA, 1972.
30. Ning, A.; Mao, W.; Chen, X.; Guo, H.; Guo, J. Precipitation Behavior of Carbides in H13 Hot Work Die Steel and Its Strengthening during Tempering. *Metals* **2017**, *7*, 70. [[CrossRef](#)]
31. Gladman, T. Precipitation hardening in metals. *Mater. Sci. Technol.* **1999**, *15*, 30–36. [[CrossRef](#)]
32. Hall, E.O. The deformation and aging of mild steel, Discussion of Metals. *Proc. Phys. Soc. Lond. B* **1951**, *64*, 747–753. [[CrossRef](#)]
33. Petch, N.J. The cleavage strength of polycrystals. *J. Iron Steel Inst.* **1953**, *174*, 25–28.
34. Fan, L.; Zhou, D.; Wang, T.; Li, S.; Wang, Q. Tensile properties of an acicular ferrite and martensite/austenite constituent steel with varying cooling rates. *Mater. Sci. Eng. A* **2014**, *590*, 224–231. [[CrossRef](#)]
35. Yong, Q. *Secondary Phases in Steels*; Metallurgical Industry Press: Beijing, China, 2006.
36. Armstrong, R. Crystal Engineering for Mechanical Strength at Nano-Scale Dimensions. *Crystals* **2017**, *7*, 315. [[CrossRef](#)]
37. Malow, T.R.; Koch, C.C. Mechanical properties, ductility, and grain size of nanocrystalline iron produced by mechanical attrition. *Metall. Mater. Trans. A* **1998**, *29*, 2285–2295. [[CrossRef](#)]
38. Karavaeva, M.V.; Kiseleva, S.K.; Ganeev, A.V.; Protasova, E.O.; Ganiev, M.M.; Simonova, L.A.; Valiev, R.Z. Superior strength of carbon steel with an ultrafine-grained microstructure and its enhanced thermal stability. *J. Mater. Sci.* **2015**, *50*, 6730–6738. [[CrossRef](#)]
39. Li, B.L.; Godfrey, A.; Meng, Q.C.; Liu, Q.; Hansen, N. Microstructural evolution of IF-steel during cold rolling. *Acta Mater.* **2004**, *52*, 1069–1081. [[CrossRef](#)]
40. Tsuji, N.; Ito, Y.; Saito, Y.; Minamino, Y. Strength and ductility of ultrafine grained aluminum and iron produced by ARB and annealing. *Scr. Mater* **2002**, *47*, 893–899. [[CrossRef](#)]
41. Xu, S.; Wang, S.; Li, S.; Cao, R.; Wu, H.; Wu, G.; Gao, J.; Feng, Q.; Li, H.; Mao, X. Achieving high strength and large elongation in a strip casting microalloyed steel by ageing treatment. *Mater. Sci. Eng. A* **2022**, *860*, 144217. [[CrossRef](#)]
42. Hansen, N. Hall–Petch relation and boundary strengthening. *Scr. Mater* **2004**, *51*, 801–806. [[CrossRef](#)]
43. Huang, T.; Shuai, L.; Wakeel, A.; Wu, G.; Hansen, N.; Huang, X. Strengthening mechanisms and Hall-Petch stress of ultrafine grained Al-0.3%Cu. *Acta Mater.* **2018**, *156*, 369–378. [[CrossRef](#)]
44. Ma, G.; Hughes, D.A.; Godfrey, A.W.; Chen, Q.; Hansen, N.; Wu, G. Microstructure and strength of a tantalum-tungsten alloy after cold rolling from small to large strains. *J. Mater. Sci. Technol.* **2021**, *83*, 34–48. [[CrossRef](#)]

**Disclaimer/Publisher’s Note:** The statements, opinions and data contained in all publications are solely those of the individual author(s) and contributor(s) and not of MDPI and/or the editor(s). MDPI and/or the editor(s) disclaim responsibility for any injury to people or property resulting from any ideas, methods, instructions or products referred to in the content.